Protein Structure and Folding:

The Role of Nonconserved Residues of *Archaeoglobus fulgidus* Ferritin on Its Unique Structure and Biophysical Properties

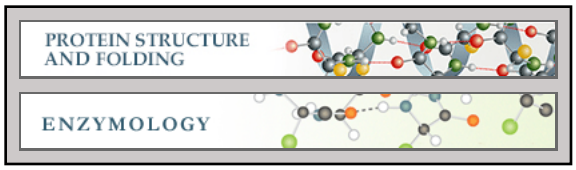

Barindra Sana, Eric Johnson, Pierre Le Magueres, Angela Criswell, Duilio Cascio and Sierin Lim

J. Biol. Chem. 2013, 288:32663-32672.
doi: 10.1074/jbc.M113.491191 originally published online September 12, 2013

THE JOURNAL OF BIOLOGICAL CHEMISTRY VOL. 288, NO. 45, pp. 32663–32672, November 8, 2013

The Role of Nonconserved Residues of *Archaeoglobus fulgidus* Ferritin on Its Unique Structure and Biophysical Properties*

Received for publication, June 4, 2013, and in revised form, August 31, 2013 Published, JBC Papers in Press, September 12, 2013, DOI 10.1074/jbc.M113.491191

Barindra Sana[‡1], **Eric Johnson**[§1,2], **Pierre Le Magueres**[¶], **Angela Criswell**[¶], **Duilio Cascio**[‖3], **and Sierin Lim**[‡4]

From the [‡]*School of Chemical & Biomedical Engineering, Division of Bioengineering, Nanyang Technological University, Singapore 637457, the* [§]*Howard Hughes Medical Institute, Division of Chemistry and Chemical Engineering, California Institute of Technology, Pasadena, California 91125,* [¶]*Rigaku Americas, The Woodlands, Texas 77381-5209, and* [‖]*UCLA-Department of Energy, Institute for Genomics and Proteomics, Los Angeles, California 90095-1570*

Background: *Archaeoglobus fulgidus* ferritin (AfFtn) assembles with unique tetrahedral symmetry and four large pores.
Results: The AfFtn K150A/R151A double mutant forms a closed octahedral assembly with reduced iron release rates relative to the tetrahedral assembly.
Conclusion: The K150A/R151A substitution alters the symmetry type of the ferritin cage.
Significance: The AfFtn can be modulated for tuning molecular release from the cavity.

Archaeoglobus fulgidus **ferritin (AfFtn) is the only tetracosameric ferritin known to form a tetrahedral cage, a structure that remains unique in structural biology. As a result of the tetrahedral (2-3) symmetry, four openings (~45 Å in diameter) are formed in the cage. This open tetrahedral assembly contradicts the paradigm of a typical ferritin cage: a closed assembly having octahedral (4-3-2) symmetry. To investigate the molecular mechanism affecting this atypical assembly, amino acid residues Lys-150 and Arg-151 were replaced by alanine. The data presented here shed light on the role that these residues play in shaping the unique structural features and biophysical properties of the AfFtn. The x-ray crystal structure of the K150A/R151A mutant, solved at 2.1 Å resolution, indicates that replacement of these key residues flips a "symmetry switch." The engineered molecule no longer assembles with tetrahedral symmetry but forms a typical closed octahedral ferritin cage. Small angle x-ray scattering reveals that the overall shape and size of AfFtn and AfFtn-AA in solution are consistent with those observed in their respective crystal structures. Iron binding and release kinetics of the AfFtn and AfFtn-AA were investigated to assess the contribution of cage openings to the kinetics of iron oxidation, mineralization, or reductive iron release. Identical iron binding kinetics for AfFtn and AfFtn-AA suggest that Fe^{2+} ions do not utilize the triangular pores for access to the catalytic site. In contrast, relatively slow reductive iron release was observed for the closed AfFtn-AA, demonstrating involvement of the large pores in the pathway for iron release.**

Ferritin is a virtually ubiquitous intracellular iron storage protein. The ferritin archetype consists of a multisubunit protein complex composed of 24 polypeptides, which self-assemble into a hollow cage structure having octahedral (4-3-2) symmetry, with external and internal diameters of ~12 and 8 nm, respectively (1, 2). Excess iron in the blood is stored in ferritin as an insoluble ferric compound that is released in soluble ferrous form during iron starvation to maintain iron homeostasis. Conversion of Fe^{2+} to Fe^{3+} in the ferritin protein complex is catalyzed by a ferroxidase center located within the hydrophilic interior of individual subunits. A mineral ferrihydrite, $[FeO(OH)]_8[FeO(H_2PO_4)]$ core is subsequently formed by accumulation of insoluble ferric iron at a nucleation site located within the ferritin cage (3–5). The ferrihydrite core may be reduced by ascorbic acid or other reducing agents to produce soluble Fe^{2+} *in vitro* (6, 7).

In general, channels of 3–5 Å diameter that are located at 3- and 4-fold molecular symmetry axes, connect the inner cavity to the ferritin surface, and are proposed as routes for inward and outward movement of ions, protons, and small molecules (3–9). The 3-fold symmetric channels are established as the main pathway for entry of Fe^{2+} ions into the cavity, whereas the function of 4-fold symmetric channels remains controversial (7, 8). Some studies have proposed the 4-fold symmetric channels as the exit route for protons and Fe^{2+} (3, 6).

The crystal structure of the *Archaeoglobus fulgidus* ferritin (AfFtn)[5] (Protein Data Bank code 1SQ3; Fig. 1) represents the first report of an archaeal ferritin structure. The report describes a tetracosameric ferritin shell with unprecedented tetrahedral (2-3) symmetry, which remains unique in structural biology (10). As a consequence of the tetrahedral assembly of the molecule, four large triangular pores (~45 Å diameter) are

* This work was supported in part by Singapore Ministry of Education Academic Research Fund Tier I Grant RG33/07 and Nanyang Technological University-National Healthcare Group Innovation Seed Grant ISG/11014.
[1] These authors contributed equally to the work.
[2] Present address: Pfizer Global Research and Development, San Diego, CA 92129.
[3] To whom correspondence may be addressed: UCLA-DOE, Inst, for Genomics and Proteomics, Los Angeles, CA 90095-1570. Tel.: 1-310-825-1551; E-mail: cascio@mbi.ucla.edu.
[4] To whom correspondence may be addressed: Div. of Bioengineering, School of Chemical and Biomedical Engineering, NTU, 70 Nanyang Dr., Block N1.3, Singapore 637457. Tel.: 65-6316-8966; Fax: +65-6791-6905; E-mail: slim@ntu.sg.

[5] The abbreviations used are: AfFtn, *A. fulgidus* ferritin; PfFtn, *P. furiosus* ferritin; SAXS, small angle x-ray scattering; RMSD, root mean square deviation.

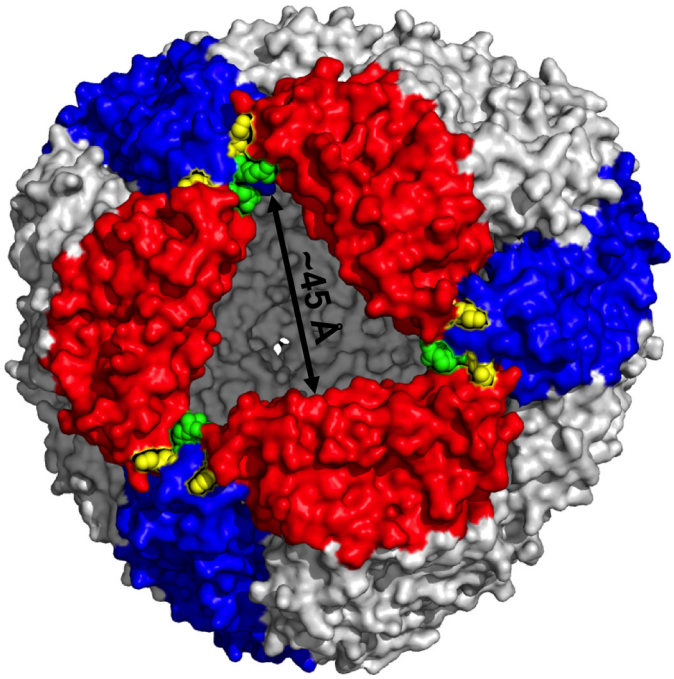

FIGURE 1. **Surface representation of the tetrahedral AfFtn showing one of the four large pores.** The Lys-150 and Arg-151 residues are drawn as space-filling representations in *yellow* and *green*, respectively. The six subunits forming the large pore are shown in *red* and *blue*.

formed, and the 4-fold symmetric channels typical of octahedral ferritins are absent. The triangular pores of AfFtn provide a potential pathway for the movement of ions and relatively larger molecules to and from the internal cavity and nucleation site. These large pores are dominated by positive electrostatic surface potential at the apices, which extends onto the interior surface of the AfFtn shell and appears to be suitable for interaction with negatively charged species.

Despite 70% sequence similarity and extremely high tertiary structure similarity (subunit RMSD = 0.422 Å), the crystal structure of the ferritin from another hypertheromphilic archaeon, *Pyrococcus furiosus* (PfFtn; Protein Data Bank code 2JD6), reveals that the PfFtn subunits assemble as a closed octahedral shell that is characteristic of ferritins (9). Sequence comparison and structural analysis of AfFtn suggest that two nonconserved amino acid residues (Lys-150 and Arg-151) are likely to play critical roles in the molecule's unique open pore assembly (10). The present study investigates the roles of these two amino acid residues on the unique structural conformation and biophysical characteristics of the AfFtn. A rationally designed AfFtn mutant has been constructed by substitution of the Lys-150 and Arg-151 residues with alanine (K150A/R151A, hereafter referred to as AfFtn-AA). The mutant is designed to test the suggestion that mutation of these key residues will act as a "symmetry switch" and induce the formation of a closed 24-mer structure with typical octahedral symmetry. Altered iron binding and release kinetics should also be observed where the presence or absence of large pores plays a role in the respective molecular mechanism. Here, we report the x-ray crystal structure of AfFtn-AA and examine the self-assembly pattern, iron loading and release relative to those of AfFtn and PfFtn.

EXPERIMENTAL PROCEDURES

Gene Expression and Protein Purification—The AfFtn gene (AF0834) was cloned into NdeI and BamHI sites of a pET-11a expression vector (Novagen). K150A/R151A mutation was constructed by PCR-based site-directed mutagenesis using duplex primers and the AF0834 gene as the template. The mutations were inserted within primer sequences. The PfFtn gene was cloned into NdeI and SalI restriction sites of the vector pET24a(+) (11). Recombinant plasmids were stored in *Escherichia coli* DH5α.

For overexpression, *E. coli* expression strain (BL21(DE3) CodonPlus-RIL) was transformed with the constructs, and protein production was done in LB medium inoculated with an overnight culture. The genes were induced for 4 h by the addition of 1 mM isopropyl β-D-thiogalactopyranoside when A_{600} was between 0.6 and 0.8. AfFtn and AfFtn-AA were purified by hydrophobic interaction chromatography after thermal purification of the cell lysate at 85 °C for 10 min following previously described method (10). Chromatography was performed on an ÄKTA-Explorer FPLC system (GE Healthcare) using HiPrep 16/10 Phenyl FF (high sub) column equilibrated with 25 mM HEPES buffer containing 50 mM NaCl and 500 mM $(NH_4)_2SO_4$, pH 7.5. The eluted fractions containing the purified protein without $(NH_4)_2SO_4$ were pooled. PfFtn was produced and purified following previously published method (9). All proteins were stored at 4 °C until use.

Protein and Iron Assay—Protein concentration was measured by bicinchoninic acid method following the manufacturer's protocol using bovine serum albumin as the standard (BCA protein assay kit; Thermo Scientific). Iron was determined spectrophotometrically by adding 20 mM dithionite to convert total iron into the ferrous form in the presence of bathophenanthroline sulfonic acid to form an iron complex following a method described by Bonomi and Pagani (12) with slight modification. Briefly, the ferritin samples were denatured by treating with 50 mM HNO_3 and mixed with 10 mM bathophenanthroline sulfonic acid, 20 mM dithionite, and 250 mM Tris buffer, pH 8.0. The mixture was incubated overnight, and iron concentration was measured from the absorbance of the complex at 538 nm (ϵ_{538} = 22.1 mM^{-1} cm^{-1}).

Self-assembly Study—Salt-mediated self-assembly was studied with apoferritin aliquots incubated overnight with different NaCl concentrations (in 25 mM HEPES buffer, pH 7.5). Molecular sizes of different AfFtn oligomers were determined by size exclusion chromatography using Superdex 200 10/300 GL column (GE Healthcare). The column was equilibrated with 25 mM HEPES, pH 7.5, containing NaCl at the same concentration in which the protein was preincubated, and the same buffer was used as mobile phase. Molecular masses of each oligomeric species were determined by comparing their elution volumes with the elution volumes of standard proteins in the same salt concentration.

The self-assembly was confirmed from the change of hydrodynamic diameter at different salt concentrations as detected by dynamic light scattering (Zetasizer Nano ZS; Malvern Instruments) technique. For salt-mediated self-assembly, the AfFtn and AfFtn-AA preparations were preincubated

TABLE 1
Statistics of x-ray data collection and atomic refinement

Protein Data Bank code	3KX9
Beamline (APS)	24-ID-C
Wavelength (Å)	0.9795
Space group	$P2_12_12_1$
Unit cell *a*, *b*, *c* (Å)	123.589, 123.596, 350.130
Resolution range (Å)	49.95–2.10 (2.18–2.10)
R_{sym} (%)[a]	7.4 (43.4)
Total number of reflections	286,468 (28,192)
Redundancy	8.3 (8.2)
Completeness (%)	92.0 (91.4)
$I/\sigma(I)$	35.59 (4.47)
Number of residues/asymmetric unit	3,964
Number of protein atoms	32,545
Number of ligand atoms	144
Number of water atoms	1116
Matthews' coefficient (Å^3/Da)	2.74
R_{work} (%)[b]	18.5
R_{free} (%)	22.7
Test set size (%), selection	5, random
RMSD bond lengths (Å)	0.007
RMSD bond angles (°)	0.952
Ramachandran angles	
Most favored (%)	97.3
Additionally allowed (%)	2.7
Generously allowed (%)	0.0
Disallowed (%)	0.0
Errat (19) overall quality factor (%)	95.35
Verify3D (20) residues with score >0.2 (%)	65.00
Average B factor for protein atoms (Å^2)	34.76
Average B factor for ligand atoms (Å^2)	54.54
Average B factor for water atoms (Å^2)	39.40

[a] $R_{sym} = 100 \times \Sigma (I - I_{mean})^2/\Sigma I^2$, where I is the observed intensity of the reflection HKL, and the sum is taken over all reflections HKL.
[b] $R_{factor} = 100 \times \Sigma||F_{obs}| - |F_{calc}||/\Sigma|F_{obs}|$, where F_{calc} and F_{obs} are the calculated and observed structure factor amplitudes, respectively. R_{work} refers to the R_{factor} for the data utilized in the refinement, and R_{free} refers to the R_{factor} for 5% of the reflections randomly chosen that were excluded from the refinement. The numbers in parentheses refer to the outer shell of data.

overnight in the presence or absence of 600 mM NaCl. The samples were equilibrated for 5 min at 25 °C prior to each measurement.

Crystal Structure Determination and Analysis—Experimental procedures for AfFtn crystal structure determination and analysis were previously reported (10). Briefly, AfFtn crystallization conditions were 27.4% PEG 400, 0.15 M $MgCl_2$, 0.1 M HEPES, pH 7.5, and a final protein concentration of 13.1 mg/ml. Crystals grew at 25 °C.

Crystals of AfFtn-AA grew at 25 °C in 41.6 mM sodium citrate, pH 5.6, 1.04 M 1,6-hexanediol, 31.25% glycerol, 166.7 mM sodium L-tartrate by hanging drop vapor diffusion. The crystals were mounted and flash frozen in liquid nitrogen without any additional cryoprotection.

Data were collected at the NE-CAT 24-ID-C Beamline at Advanced Photon Source (Argonne National Laboratory) and processed with DENZO and SCALEPACK (13). The structure was solved by molecular replacement with PHASER (14) using the open pore structure of AfFtn with zinc bound (Protein Data Bank code 1S3Q) as the search model. Manual building of the model was done in Coot (15) and refined in REFMAC (16) and PHENIX (17). The final model was validated with PROCHECK (18), ERRAT (19), and Verify3D (20) through the NIH-MBI SAVS server. All graphic representations of molecular structures were prepared with PyMOL (21). Crystallographic statistics are summarized in Table 1, and the data are deposited in the Protein Data Bank (code 3KX9).

Secondary structure comparisons were performed using secondary structure matching program in Coot (22). Surface area calculation was performed on the protein interfaces, surfaces, and assemblies online portal (PDBePISA).

TABLE 2
SAXS data collection and scattering-derived parameters for the three concentrations of the AfFtn and AfFtn-AA samples

Data collection parameters	
Instrument	BioSAXS-1000 (Rigaku)
Beam geometry	700 μm × 200 μm (at sample position) 500 μm × 500 μm (at detector)
Wavelength (Å)	1.5418
q range (Å^{-1})	0.008–0.65
Exposure time (min)	30
Temperature (K)	277
Software employed	
Primary data reduction	SAXSLab
Data processing	PRIMUS
Ab initio analysis	DAMMIF
Validation and averaging	DAMAVER
Rigid body modeling	SUPCOMB
Computation of model intensities	CRYSOL
Three-dimensional graphics representation	PyMOL

SAXS Studies—SAXS data were collected on a Rigaku BioSAXS-1000 system configured with a Rigaku FR-E+ Superbright rotating anode generator operating at 2.475 kW. The BioSAXS-1000 system is a two-dimensional Kratky SAXS camera that utilizes a point focus source, a Kratky block for beam collimation, and a Dectris Pilatus 100K detector. The Pilatus 100K is a hybrid pixel array detector that provides high sensitivity and low readout noise, both of which are ideal for measuring the very low SAXS signal provided by most macromolecules in solution. The sample to camera distance is ~500 mm, and the q range is 0.008 – 0.65 Å^{-1}. The BioSAXS-1000 beam path was evacuated to reduce absorption of the scattered x-rays by air. The data collection and scattering-derived parameters are shown on Table 2.

To test for concentrations effects, the sample was serially diluted 50 and 25% with buffer (25 mM HEPES, pH 7.5, containing 500 mM NaCl and 4% glycerol). Prior to SAXS measurements, each sample was centrifuged for 10 min at 4 °C at 10,000 rpm. Then ~20 μl of sample was pipetted into 1.0-mm quartz capillary cells that were sealed at each end with screw caps and O-rings for measurement under vacuum. Both buffer and sample solutions were measured in the same capillary cell for proper buffer subtraction. For each sample and buffer measurement, two scans of 30 min were collected. All data were collected at 4 °C.

Following direct beam and sample to detector distance calibration with a silver behenate standard, the SAXS images from the x-ray detector were azimuthally averaged to obtain one-dimensional scattering profiles using *SAXSLAb*. Duplicate scattering profiles were averaged together, and the averaged buffer profiles were subtracted from the average sample profiles using *PRIMUS* (23). The resulting scattering data are shown as a function of increasing q. Following buffer subtraction, Guinier plots were prepared using *PRIMUS* (23) for each sample dilution to assess sample quality, determine the forward scattering intensity, $I(0)$, and determine the radius of gyration, R_g. Low resolution data to $q < 1.3\ R_g$ were used to define the Guinier region and determine R_g. *GNOM* was used to calculate the indirect Fourier transformation of the scattering data from reciprocal space to real space as expressed in the pair distance

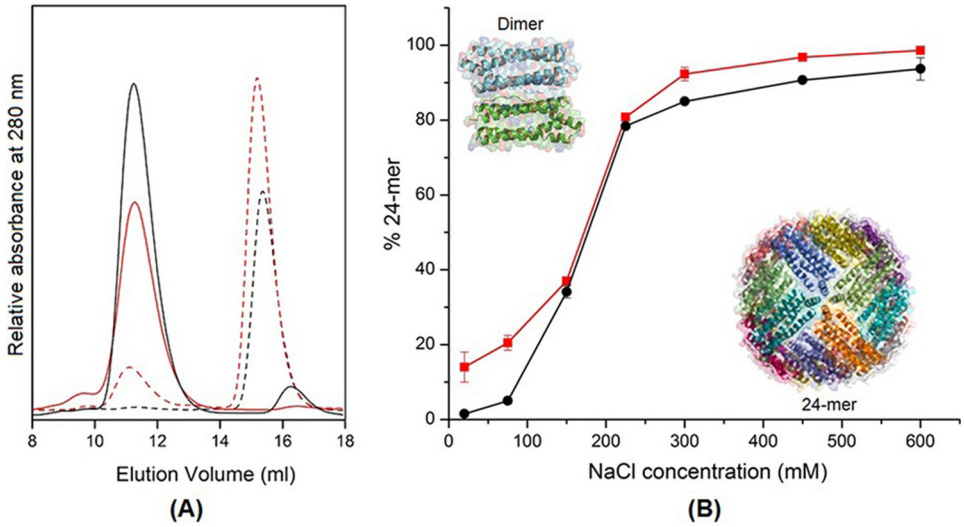

FIGURE 2. *A*, size exclusion chromatogram showing elution volumes of different oligomeric species of AfFtn (*black*) and AfFtn-AA (*red*) in the presence of 600 mM NaCl (*solid lines*) and 20 mM NaCl (*dashed lines*). A systematic shift toward higher elution volume was observed for both experimental samples (*solid lines*) and molecular mass standards (not shown) at 600 mM NaCl relative to that in 20 mM NaCl. *B*, distribution of 24-mer in AfFtn (*black*) and AfFtn-AA (*red*) solutions in the presence of different NaCl concentrations as determined by size exclusion chromatography.

distribution function, $P(r)$. The R_g and $I(0)$ from the $P(r)$ are also reported. The molecular masses were estimated using the experimentally determined forward scattering value, $I(0)$, using a glucose isomerase standard and from the calculated Porod volume,

$$V = 2\pi^2 \cdot (I(0)/Q) \qquad \text{(Eq. 1)}$$

by using the program *datPOROD* (24) and the web service *SAXSMoW* (25). Ten low resolution *ab initio* shape models were calculated using the program DAMMIF (24).

These models were subsequently aligned and averaged with the programs SUPCOMB (26) and DAMAVER (27). The filtered SAXS model and the sample crystal structures were superimposed with *SUPCOMB* (26). The dry volume and partial specific volume were calculated from the sequence of the monomeric species using the web service (28).

Iron Binding—Iron loading (mineralization) of ferritin was performed following a previously described method (4). Briefly, freshly prepared ferrous sulfate solution in 0.1% HCl was added to apoferritin solution followed by incubation for 1 h at room temperature and overnight at 4 °C.

Binding kinetics was studied in dilute protein solutions (0.01 mg/ml) to avoid fast autoxidation at higher Fe^{2+} concentrations. The reaction was monitored colorimetrically by measuring the absorbance increase at 315 nm. The reaction was started by addition of 10 μl of freshly prepared 10 mM ferrous sulfate solution in 0.1% HCl to 1 ml of 0.01 mg/ml ferritin solution (in 100 mM HEPES, pH 7.0) preincubated at 20 °C in a temperature-controlled spectrophotometer. The binding kinetics of AfFtn and AfFtn-AA was compared with that of PfFtn.

Iron Release—The iron release profiles of mineralized ferritins were studied at 70 °C in the presence of 10 mM ascorbate (reducing agent) and 1 mM ferrozine. The final protein concentration was maintained at 0.05 mg/ml in 0.1 M HEPES, pH 7.0. Mineralized ferritin solution (loaded with ~1200 Fe/24-mer) was incubated with 1 mM ferrozine in a temperature-controlled spectrophotometer. The reaction was started by addition of 10 μl of 1 M ascorbate, and iron release was studied by monitoring the formation of Fe^{2+}-ferrozine complex at 562 nm. Iron release kinetics of AfFtn and AfFtn-AA was compared with PfFtn.

RESULTS AND DISCUSSION

AfFtn and AfFtn-AA Show Comparable Self-assembly Pattern—AfFtn has been shown to exist primarily as dimer and fully assembled 24-mer at 20 and 600 mM NaCl concentrations, respectively (10, 29). Size exclusion chromatography and dynamic light scattering studies at different salt concentrations suggest that the self-assembly of AfFtn-AA is also dependent on ionic strength. At all ionic strengths tested (ranging from 20 to 600 mM) AfFtn and AfFtn-AA eluted primarily in two peaks corresponding to dimer (~45 kDa) and 24-mer (~490 kDa) (Fig. 2*A*). No other oligomeric species corresponding to theoretical intermediates in the self-assembly process were observed. For both AfFtn and AfFtn-AA, the 24-mer to dimer ratio gradually increased with increasing ionic strength, but the AfFtn-AA consistently contained a higher proportion of 24-mer when compared with AfFtn (Fig. 2). At low ionic strength, AfFtn eluted as a single peak corresponding to dimer, whereas ~15% of the AfFtn-AA was eluted as a 24-mer. In buffer containing 600 mM NaCl, 100% of the AfFtn-AA preparation was converted to 24-mer, whereas ~4% of AfFtn remained in the dimeric state. Further supporting the observed salt-mediated self-assembly of these proteins, increased hydrodynamic diameters of AfFtn and AfFtn-AA were also observed in dynamic light scattering analysis after addition of 600 mM NaCl (Fig. 3). These observations indicate that the replacement of Lys-150 and Arg-151 amino acid residues has a minimal effect on the solution properties of AfFtn-AA. It is also to be noted that the salt-mediated self-assembly is reversible and operates in a very similar manner for both AfFtn and AfFtn-AA. The small increase in the ratio of 24-mer to dimer in solutions of AfFtn-AA indicates a shift in equilibrium,

away from dimeric species, most likely because of a lower energy 24-mer end product.

Analysis of crystal structures identified several hydrophobic contacts at the subunit interfaces that appear to be important for stabilization of the self-assembled 24-mer structures of AfFtn and AfFtn-AA. Salt-mediated self-assembly is caused by enhanced hydrophobic interactions at high ionic strength, and a clear shift is observed in the oligomeric state with increased NaCl concentrations (Fig. 2*B*). The reversible salt-mediated process supports hydrophobic interactions as a key force in shifting the dimeric structures to 24-meric cage. In addition, substitution of hydrophilic Lys-150 and Arg-151 residues of AfFtn with hydrophobic alanine in AfFtn-AA fits with the observation of a shift in equilibrium toward 24-mer in AfFtn-AA compared with wild-type AfFtn. The substitution removes destabilizing forces (*i.e.*, steric clashes and repulsive charges) and allows enhanced interactions between subunits in the assembled AfFtn-AA, hence increasing the proportion of 24-mer in AfFtn-AA as compared with the wild-type AfFtn.

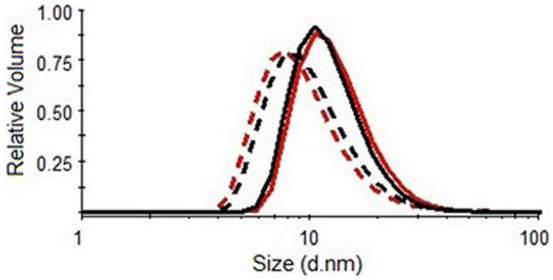

FIGURE 3. **Hydrodynamic diameters of AfFtn (*black*) and AfFtn-AA (*red*) in the presence of 600 mM NaCl (*solid lines*) and 20 mM NaCl (*dashed lines*) as determined by dynamic light scattering.** The hydrodynamic diameters were measured as follows: AfFtn, 9.4 nm (20 mM) and 14.0 nm (600 mM); and AfFtn-AA, 9.2 nm (20 mM) and 14.0 nm (600 mM).

The Crystal Structure of AfFtn-AA Indicates Rearrangement of Molecular Quaternary Symmetry—Based on the crystal structure of AfFtn, the amine side chain of the AfFtn Lys-150 residue forms a hydrogen bond with the backbone O at Met-111, an interaction that likely stabilizes the unusual structure with tetrahedral symmetry (Figs. 4*A* and 5*A*). The AfFtn Arg-151 side chain is positioned such that it would prohibit assem-

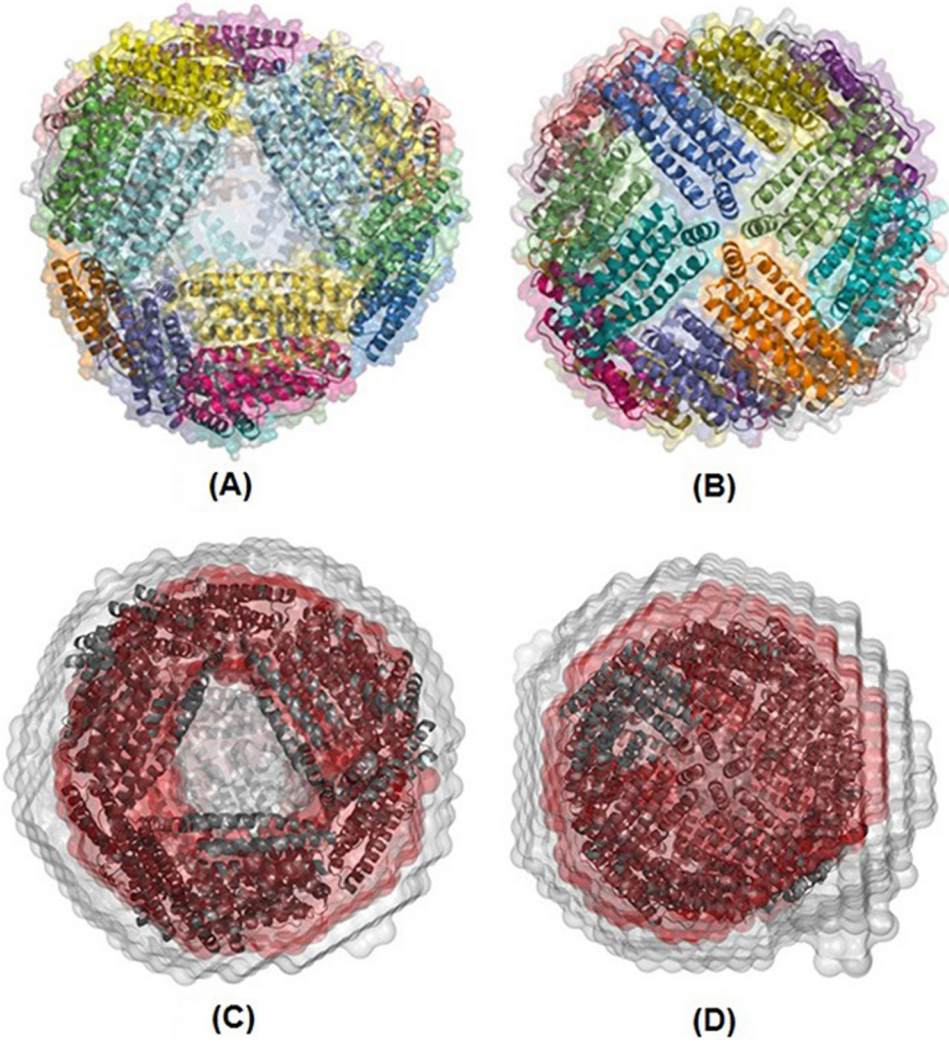

FIGURE 4. *A* and *B*, crystal structure of AfFtn (*A*) and AfFtn-AA (*B*). *C* and *D*, overlay of the filtered (*red*) and averaged (*gray*) envelopes (both calculated from SAXS data) of AfFtn (*C*) and AfFtn-AA (*D*) with the respective crystal structures (*dark maroon*). The averaged envelope (or bead model) is produced by DAMAVER and represents the total spread of all the individual superposed models. The filtered envelope is produced by DAMFILT, which removes low occupancy and loosely connected atoms from the averaged envelope to generate a compact, more probable model.

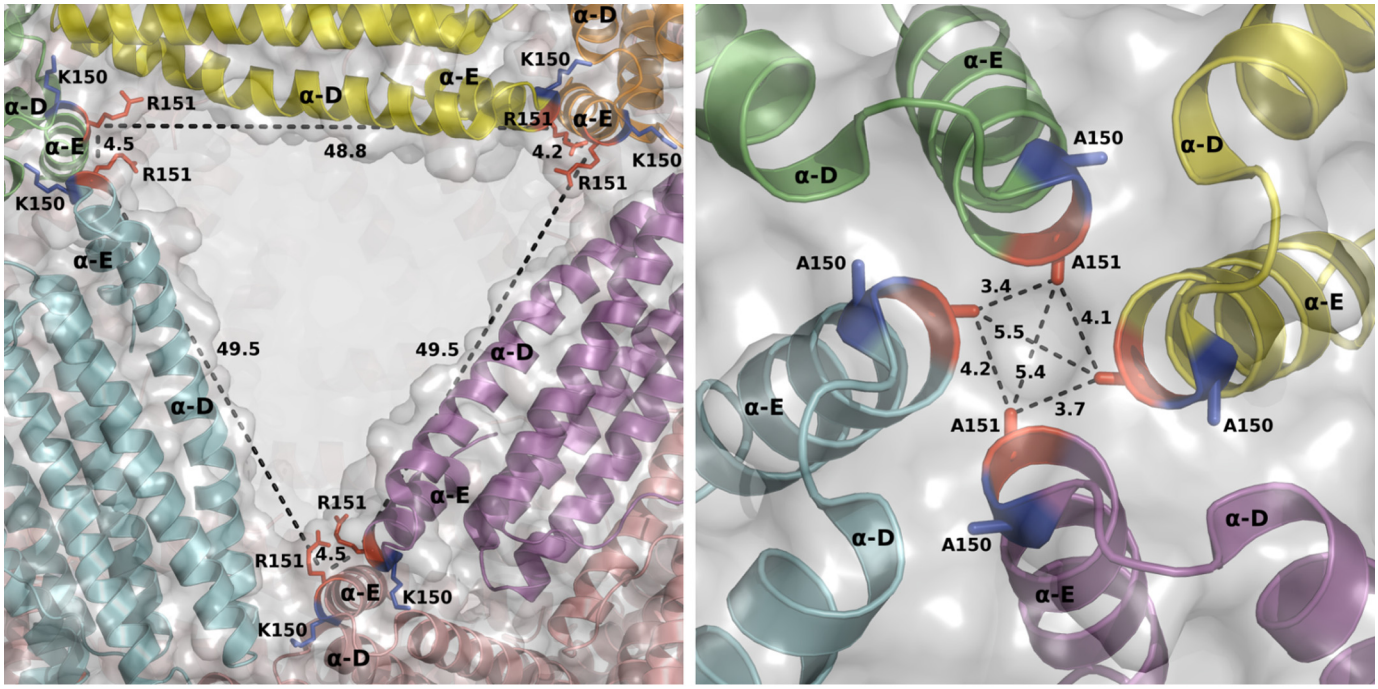

FIGURE 5. **Location of mutation sites in AfFtn and AfFtn-AA.** *A*, detailed view of a large pore from the tetrahedral AfFtn showing locations of Lys-150 and Arg-151 residues drawn as *blue* and *red sticks*, respectively. *Numbers* indicate intermolecular distance (Å) between Arg-151 Cβ atoms from adjacent monomers and are illustrated by *black dashes*. *B*, detailed view of packing at the 4-fold interface of AfFtn-AA illustrating the proximity of Ala-150 and Ala-151 residues from adjacent monomers in the octahedral assembly. *Numbers* indicate distance (Å) between adjacent Ala-151 Cβ atoms. Alanine residues at positions 150 and 151 are drawn as *sticks* with *colors* as in *A*.

bly of a closed octahedral structure by sterically blocking association of helices at the octahedral 4-fold interface (10). Moreover, these nonconserved amino acid residues contribute to the formation of positively charged clusters located at apices of the triangular open pores. Replacement of these bulky positively charged side chains with the small uncharged side chain of an alanine residue is hypothesized to decrease the positive surface potential at the triangle apices. Therefore, Lys-150 and Arg-151 residues seem critical for the unique open pore structure of AfFtn.

Replacement of the two key amino acids causes a massive rearrangement of the quaternary structure; cage assembly is switched from tetrahedral in AfFtn to octahedral symmetry for the AfFtn-AA. The crystal structure of AfFtn-AA (Protein Data Bank code 3KX9) clearly demonstrates this symmetry switch as a closed protein cage with octahedral symmetry is observed (Fig. 4*B*).

In AfFtn, pairs of adjacent Arg-151 residues are located ~49 Å apart at each apex of the large triangular pores (Figs. 1 and 5*A*). In the AfFtn-AA crystal structure, four mutant residues (Ala-151) are rearranged to pack closely (~4 Å apart) at the 4-fold symmetry interfaces (Fig. 5*B*). This packing appears to stabilize the closed structure through Ala-151–Ala-151 hydrophobic interactions. The closed structure has a slightly smaller diameter than AfFtn based on the crystal structures. The calculated accessible surface area for AfFtn-AA is also smaller (146,140 Å^2) compared with AfFtn (156,450 Å^2) but has a larger buried surface area (77,000 Å^2) compared with AfFtn (64,950 Å^2). The decrease in the accessible surface area from AfFtn to AfFtn-AA may serve as an approximate measurement of the free energy difference between the two types of cages (30, 31). Thus, by closing the triangular pore in AfFtn-AA, the buried surface area is increased, and the octahedral cage is thermodynamically more stable than the tetrahedral AfFtn cage. The direct evidence of the increased stability is the observed shift in the solution equilibrium.

SAXS data reveal that the overall shape and size of AfFtn and AfFtn-AA in solution are consistent with their respective crystal structures (Fig. 4, *C* and *D*). Specifically, structural parameters (D_{max}, R_g, and molecular mass) calculated from the SAXS data are consistent with those from the crystal structure (Table 3). The structural parameters are smaller for AfFtn-AA relative to AfFtn by 3–6 and 2–4 Å, respectively, across the concentration range. This would be consistent with a closed conformation for AfFtn-AA *versus* an open conformation for AfFtn. SAXS profiles and Kratky plots show several peaks, as expected for hollow spheres. Also, the shape of the pair-distance distribution function for both AfFtn and AfFtn-AA is typical of hollow spheres, with a maximum shifted toward a distance larger than $D_{max}/2$ (Fig. 6).

Quaternary Structures of the AfFtn-AA Resemble PfFtn More Closely than AfFtn—Hexamer is a widely proposed intermediate in self-assembly of ferritin cages despite the absence of any experimental observations (9, 10, 32). The structural conformation of hexameric intermediate may reflect the symmetry of 24-meric ferritin cage. Structural superimposition of AfFtn, AfFtn-AA, and PfFtn monomers, dimers, and hexamers shows that the primary, secondary, and tertiary structures of AfFtn-AA are closely related to AfFtn and PfFtn (Fig. 7). As expected for the monomer, AfFtn-AA is more structurally related to AfFtn

TABLE 3
Comparison of D_{max}, R_g values, and molecular mass calculated from the SAXS data and the crystal structure of apo AfFtn and AfFtn-AA

	SAXS				
	8 mg/ml	4 mg/ml	2 mg/ml	Average	Structure
D_{max} (Å)					
AfFtn	131	133	133	133	142[a]
AfFtn-AA	129	128	130	129	136[a]
R_g (Å) from $P(r)$					
AfFtn	55.46	55.63	55.55	55.55	57.25[b]
AfFtn-AA	53.18	53.26	53.42	53.29	53.61[b]
Molecular mass (kDa) from Porod volume/$I(0)$/SAXSMoW					
AfFtn	425.1/435.0/459.5	466.9/433.9/482.7	440.5/436.8/471.2	441.2/435.2/471.1	487.6[c]
AfFtn-AA	442.2/436.3/463.8	459.3/438.2/479.9	464.1/456.8/488.5	455.2/443.9/477.4	484.2[c]

[a] Calculated from the crystal structure using both CRYSOL and Moleman2.
[b] Calculated from the crystal structure using CRYSOL.
[c] Calculated from the sequence using ProtParam tool.

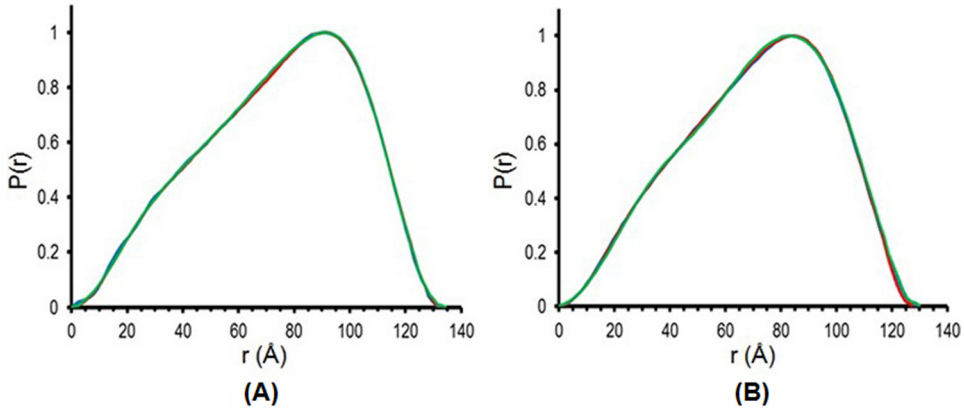

FIGURE 6. **Normalized pair-distance distribution function plots for three concentrations of AfFtn (*A*) and AfFtn-AA (*B*) obtained from 30-min exposures.** *Blue*, 8 mg/ml; *red*, 4 mg/ml; *green*, 2 mg/ml protein concentration. The shape of the pair-distance distribution function for both AfFtn and AfFtn-AA is typical of hollow spheres. Average D_{max} values of AfFtn and AfFtn-AA are calculated as 133 and 129 Å, respectively.

(RMSD = 0.393 Å) than PfFtn (RMSD = 0.648 Å). However, at the level of quaternary subassembly components (dimers and hexamers), AfFtn-AA is actually more closely related to PfFtn (dimer and hexamer RMSDs = 0.775 and 0.881 Å, respectively) than AfFtn (dimer and hexamer RMSDs = 0.820 and 1.066 Å, respectively). Despite relatively low similarity in primary, secondary, and tertiary structure, the quaternary structure of the octahedral AfFtn-AA and PfFtn resemble each other most closely, both in the symmetry class of the 24-mer and in the structural relatedness of their quaternary dimeric and hexameric building blocks. In contrast, although AfFtn-AA and AfFtn have 99% sequence identity and virtually identical subunit structure, the quaternary building blocks are less structurally related, relative to PfFtn, and the cages assemble with divergent symmetry (octahedral *versus* tetrahedral).

The Large Triangular Pores Are Involved in the Ascorbate Transport to the Core and Affect the Release Rate but Not the Nucleation Rate—Ferritin is the iron storage protein with oxidoreductase activity. It buffers intracellular and extracellular iron levels by highly coordinated activity of specific ion channels and catalytic centers. Fe^{2+} ions pass through openings on the protein surface to the catalytic centers and are oxidized to Fe^{3+} ions that move to the nucleation site for subsequent bulk mineralization (7). Comparative studies of iron binding/release kinetics of AfFtn and AfFtn-AA were performed to elucidate the role of the distinct triangular pores of AfFtn in the iron transport pathway. The iron binding and release kinetics of AfFtn and AfFtn-AA were also compared with another archaeal ferritin, PfFtn. Fig. 8*A* shows that iron binding kinetics in all three ferritins have more than one phase. The initial fast reaction is due to immediate oxidation of irons at the ferroxidase center that is followed by a subsequent slower oxidation phase at the nucleation site within the ferritin cavity. The latter phase requires transport of Fe^{2+} ion into the cavity from the external environment. Experiments show virtually identical iron binding kinetics for both AfFtn and AfFtn-AA and suggest that the triangular pores do not play a significant role in the mechanism of Fe^{2+} oxidation. Ion transport through protein is governed by charge distribution of specific ion channels. Fe^{2+} ion intake in ferritin takes place through a very specific pathway, *i.e.*, the hydrophilic 3-fold symmetric channels, which are lined by negatively charged amino acids. From the crystal structure data of frog ferritin, Tosha *et al.* (7) reported that metal ions need to follow specific ion channels from the 3-fold openings with highly conserved residues to access the catalytic site at the ferritin interior. They showed that the movement of Fe^{2+} ion from the pore opening is guided by the charge distribution of the channel. Mutation of several amino acids on the 3-fold symmetric channel of frog M-ferritin showed that specific residues are essential in each step of Fe^{2+} ion mobility from the channel opening to the nucleation site (8, 33). AfFtn has a second potential route for Fe^{2+} ion entry, *i.e.*, the negatively charged channels previously described as "A" channels (10). These channels are located between the noncrystallographic symmetry axis and

the large triangular pore. They extend to the ferritin interior and are large enough for transport of Fe^{2+} ions. Although negatively charged 3-fold symmetric channels and A channels of AfFtn appear suitable for inward movement of Fe^{2+} ion, the charge distribution of the large triangular pores may not be favorable for this purpose. Positive electrostatic potential of the triangle apices is extended from the exterior surface of AfFtn, through the pore opening, and onto the interior surface of the AfFtn shell (10). Reasonably, this positive surface potential is unlikely to favor passage of any positively charged moiety through these pores. However, slower Fe^{2+} oxidation in PfFtn may be due to the difference in electrostatic charge in the 3-fold channels of the ferritins isolated from two different species. The 3-fold channels of PfFtn are reported to be less hydrophilic in comparison with that of AfFtn, and this may cause lower affinity of Fe^{2+} ion to the 3-fold symmetric channels of PfFtn than 3-fold symmetric channels of AfFtn or AfFtn-AA (9).

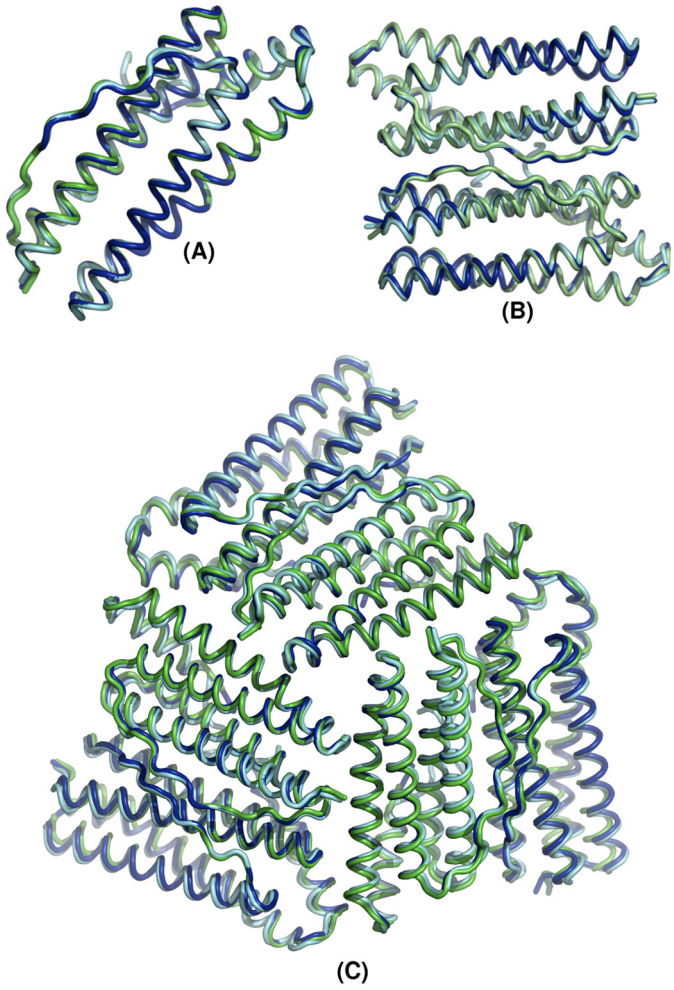

FIGURE 7. **Structural similarity of archeal ferritin subunits and oligomeric assemblies.** *A*, superpositioning of AfFtn (*green*), AfFtn-AA (*blue*), and PfFtn (*cyan*) monomers performed using Coot secondary structure matching. The AfFtn-AA monomer is more structurally related to the AfFtn monomer (RMSD = 0.393 Å) than the monomer of PfFtn (RMSD = 0.648 Å). At the level of quaternary structure, the AfFtn-AA is more structurally related to the PfFtn. *B*, dimers of AfFtn-AA superimposed on those of PfFtn and AfFtn yield RMSDs of 0.775 and 0.881 Å, respectively. *C*, superpositioning of hexamers also yields smaller RMSDs for AfFtn-AA and PfFtn (0.820 Å) compared with AfFtn-AA and AfFtn (1.066 Å).

Fig. 8*B* shows the iron release kinetics by ascorbate-mediated Fe^{3+} reduction. The initial iron release rates of AfFtn, AfFtn-AA, and PfFtn were calculated to be 90, 70, and 57 μM min^{-1}, respectively. The iron release rate of AfFtn-AA is slower than that of AfFtn, which suggests involvement of the triangular pores in reductive iron release from the AfFtn core. However, the contribution of these pores in the iron transport process is yet to be rigorously established. These pores could be used for transport of negatively charged ascorbate to the nucleation site. The relatively small decrease in the iron release rate of the closed AfFtn-AA indicates a minor contribution of the large pores under these conditions. A much larger change would be expected if the triangular pores provide a substantial pathway for ascorbate transport or if transport is not rate-limiting. Similar results were obtained using another reducing agent, *i.e.*, NADH (data not shown). Ascorbate-mediated reduction of ferric core is a common observation in many archetypal ferritins, which further supports the role of the large triangular pores of AfFtn as a route that is additional to the narrow channels generally used for ascorbate transport in ferritins. Like any typical octahedral ferritin, AfFtn-AA may utilize 3- or 4-fold channels for ascorbate transport.

Reductive iron release from ferritin core is a complex process that depends on access of the reducing agent to the ferric core and the transport of reduced Fe^{2+} ion from the interior to the channel openings (34, 35). The existing literature evidence suggests that both 3- and 4-fold channels are associated with the reductive iron release mechanism (3, 6, 36, 37). The 4-fold

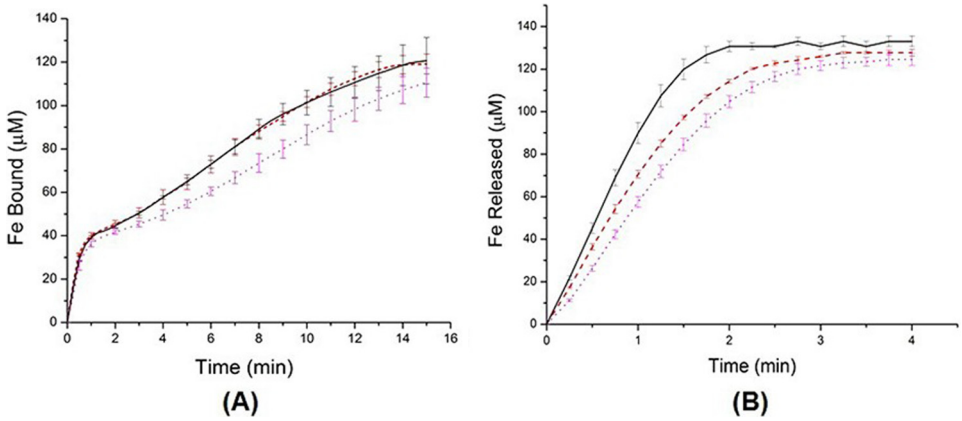

FIGURE 8. *A* and *B*, iron binding kinetics (*A*) and ascorbate-mediated iron release kinetics (*B*) of AfFtn (*black*, *solid line*), AfFtn-AA (*red*, *dashed line*), and PfFtn (*magenta*, *dotted line*).

channels were predicted as the route for proton and Fe^{2+} ion transport during mineralization and demineralization (3, 6). In two different studies, the 3-fold channels of horse ferritin were locally unfolded by mutation of conserved amino acids in the 3-fold channels. The mutations resulted in increased Fe^{2+} release rates, and the authors proposed involvement of the 3-fold channels in the mechanism of reductive iron release (36, 37). Another study observed iron release as a multistep procedure involving hydrolysis of Fe-O/OH-Fe bridges, chelation of iron inside the ferritin cage, and/or transfer of iron to the chelator outside the ferritin (4). This study further described the ferritin channel as a gated pore. Control of reductive iron release was explained by controlled access of reducing/chelating agents to the ferric core by altering the structure of these gated pores.

Based on the charge distribution of the triangular pores of AfFtn and our experimental observations, we hypothesize that these pores are used for entry of negatively charged ascorbate but have no role in the transport of positively charged Fe^{2+} ion. The large triangular pores allow faster ascorbate transport to the AfFtn core and, hence, an increased rate of Fe^{3+} reduction compared with AfFtn-AA. The closed octahedral cage of AfFtn-AA limits access of ascorbate into the ferritin interior, which leads to relatively slow rates of Fe^{3+} reduction. Considering the major structural differences in tetrahedral and octahedral assemblies, it is possible that features distinct from the pores contribute to the slower iron release rate observed in AfFtn-AA. Further studies will be required to verify the precise molecular components involved in the complex process of iron release from these fascinating iron storage proteins.

Conclusion—Using x-ray crystal structures, SAXS, and kinetic data, we demonstrate that the triangular pores of AfFtn are not artifacts of crystallization and that the Lys-150 and Arg-151 residues are critical for stabilization of the open pore tetrahedral structure of AfFtn. The data presented here further indicate that the large pores are involved in reductive iron release from AfFtn. Substitution of the bulky positively charged side chains of Lys-150 and Arg-151 with the small hydrophobic side chain of alanine results in a massive rearrangement in the quaternary structure and a switch from tetrahedral to octahedral symmetry. The mutations remove steric clashing and provide enhanced hydrophobic interactions at the 4-fold interface, allowing subunits to self-assemble into a closed archetypal ferritin cage with slightly smaller dimensions compared with the wild type. With the caveat of unavoidable differences between conditions in crystallization and solution experiments, the structural parameters obtained from SAXS are consistent with those obtained from the crystal structures.

Analysis of the crystal structures and the observation of self-assembly in conditions of high ionic strength also indicate hydrophobic interactions as key forces that stabilize the cage structures of both AfFtn and AfFtn-AA. Elimination of the large triangular pores results in slower reduction of Fe^{3+} core but does not affect the rate of Fe^{2+} oxidation and suggests that these pores are not involved in Fe^{2+} ion transport. However, understanding the exact function of these pores and their exact role in the reductive release of the Fe^{3+} core will require further research.

Acknowledgments—We thank Prof. Imke Schroeder (UCLA) and Prof. Wilfred R. Hagen (Delft University of Technology) for the generous gifts of AfFtn, AfFtn-AA, and PfFtn plasmids, respectively. We thank M. Sawaya and the UCLA-DOE X-ray Crystallography Core Facility, which is supported by DOE Grant DE-FC02-02ER63421. We thank M. Capel, K. Rajashankar, N. Sukumar, J. Schuermann, I. Kourinov, and F. Murphy (Northeastern Collaborative Access Team Beamline 24-ID at Advanced Photon Source, which is supported by National Center for Research Resources Grant 5P41RR015301-10 and National Institute of General Medical Sciences Grant 8 P41 GM103403-10 from the National Institutes of Health). Use of the Advanced Photon Source is supported by the Department of Energy under Contract DE-AC02-06CH11357.

REFERENCES

1. Theil, E. C. (1987) Ferritin: Structure, gene regulation, and cellular function in animals, plants, and microorganisms. *Annu. Rev. Biochem.* **56,** 289–315
2. Theil, E. C., Liu, X. S., and Tosha, T. (2008) Gated pores in the ferritin protein nanocage. *Inorg. Chim. Acta* **361,** 868–874
3. Takahashi, T., and Kuyucak, S. (2003) Functional properties of threefold and fourfold channels in ferritin deduced from electrostatic calculations. *Biophys. J.* **84,** 2256–2263
4. Liu, X., Jin, W., and Theil, E. C. (2003) Opening protein pores with chaotropes enhances Fe reduction and chelation of Fe from the ferritin biomineral. *Proc. Natl. Acad. Sci. U.S.A.* **100,** 3653–3658
5. Levi, S., Luzzago, A., Cesareni, G., Cozzi, A., Franceschinelli, F., Albertini, A., and Arosio, P. (1988) Mechanism of ferritin iron uptake. Activity of the H-chain and deletion mapping of the ferro-oxidase site. A study of iron uptake and ferro-oxidase activity of human liver, recombinant H-chain ferritins, and of two H-chain deletion mutants. *J. Biol. Chem.* **263,** 18086–18092
6. Douglas, T., and Ripoll, D. R. (1998) Calculated electrostatic gradients in recombinant human H-chain ferritin. *Protein Sci.* **7,** 1083–1091
7. Tosha, T., Ng, H.-L., Bhattasali, O., Alber, T., and Theil, E. C. (2010) Moving metal ions through ferritin-protein nanocages from three-fold pores to catalytic sites. *J. Am. Chem. Soc.* **132,** 14562–14569
8. Haldar, S., Bevers, L. E., Tosha, T., and Theil, E. C. (2011) Moving iron through ferritin protein nanocages depends on residues throughout each four α-helix bundle subunit. *J. Biol. Chem.* **286,** 25620–25627
9. Tatur, J., Hagen, W. R., and Matias, P. M. (2007) Crystal structure of the ferritin from the hyperthermophilic archaeal anaerobe *Pyrococcus furiosus*. *J. Biol. Inorg. Chem.* **12,** 615–630
10. Johnson, E., Cascio, D., Sawaya, M. R., Gingery, M., and Schröder, I. (2005) Crystal structures of a tetrahedral open pore ferritin from the hyperthermophilic Archaeon *Archaeoglobus fulgidus*. *Structure* **13,** 637–648
11. Matias, P. M., Tatur, J., Carrondo, M. A., and Hagen, W. R. (2005) Crystallization and preliminary X-ray characterization of a ferritin from the hyperthermophilic archaeon and anaerobe *Pyrococcus furiosus*. *Acta Crystallogr. Sect. F Struct. Biol. Cryst. Commun.* **61,** 503–506
12. Bonomi, F., and Pagani, S. (1986) Removal of ferritin-bound iron by DL-dihydrolipoate and DL-dihydrolipoamide. *Eur. J. Biochem.* **155,** 295–300
13. Otwinowski, Z., and Minor, W. (1997) Processing of x-ray diffraction data collected in oscillation mode. *Methods Enzymol.* **276,** 307–326
14. McCoy, A. J., Grosse-Kunstleve, R. W., Adams, P. D., Winn, M. D., Storoni, L. C., and Read, R. J. (2007) Phaser crystallographic software. *J. Appl. Crystallogr.* **40,** 658–674
15. Emsley, P., and Cowtan, K. (2004) Coot. Model-building tools for molecular graphics. *Acta Crystallogr. D Biol. Crystallogr.* **60,** 2126–2132
16. Vagin, A. A., Steiner, R. A., Lebedev, A. A., Potterton, L., McNicholas, S., Long, F., and Murshudov, G. N. (2004) REFMAC5 dictionary. Organization of prior chemical knowledge and guidelines for its use. *Acta Crystallogr. D Biol. Crystallogr.* **60,** 2184–2195
17. Adams, P. D., Afonine, P. V., Bunkóczi, G., Chen, V. B., Davis, I. W., Echols, N., Headd, J. J., Hung, L. W., Kapral, G. J., Grosse-Kunstleve, R. W.,

McCoy, A. J., Moriarty, N. W., Oeffner, R., Read, R. J., Richardson, D. C., Richardson, J. S., Terwilliger, T. C., and Zwart, P. H. (2010) PHENIX. A comprehensive Python-based system for macromolecular structure solution. *Acta Crystallogr. D Biol. Crystallogr.* **66,** 213–221
18. Laskowski, R. A., MacArthur, M. W., Moss, D. S., and Thornton, J. M. (1993) PROCHECK. A program to check the stereochemical quality of protein structures. *J. Appl. Crystallogr.* **26,** 283–291
19. Colovos, C., and Yeates, T. O. (1993) Verification of protein structures. Patterns of nonbonded atomic interactions. *Protein Sci.* **2,** 1511–1519
20. Lüthy, R., Bowie, J. U., and Eisenberg, D. (1992) Assessment of protein models with three-dimensional profiles. *Nature* **356,** 83–85
21. *The PyMOL Molecular Graphics System*, Version 1.3. Schrödinger, LLC.
22. Krissinel, E., and Henrick, K. (2004) Secondary-structure matching (SSM), a new tool for fast protein structure alignment in three dimensions. *Acta Crystallogr. D Biol. Crystallogr.* **60,** 2256–2268
23. Konarev, P. V., Volkov, V. V., Sokolova, A. V., Koch, M. H. J., and Svergun, D. I. (2003) PRIMUS. A Windows PC-based system for small-angle scattering data analysis. *J. Appl. Crystallogr.* **36,** 1277–1282
24. Petoukhov, M. V., Konarev, P. V., Kikhney, A. G., and Svergun, D. I. (2007) ATSAS 2.1. Towards automated and web-supported small-angle scattering data analysis. *J. Appl. Crystallogr.* **40,** s223–s228
25. Fischer, H., de Oliveira Neto, M., Napolitano, H. B., Polikarpov, I., and Craievich, A. F. (2010) The molecular weight of proteins in solution can be determined from a single SAXS measurement on a relative scale. *J. Appl. Crystallogr.* **43,** 101–109
26. Kozin, M. B., and Svergun, D. I. (2001) Automated matching of high-and low-resolution structural models. *J. Appl. Crystallogr.* **34,** 33–41
27. Volkova, V. V., and Svergun, D. I. (2003) Uniqueness of ab initio shape determination in small-angle scattering. *J. Appl. Crystallogr.* **36,** 860–864
28. Voss, N. R., and Gerstein, M. (2005) Calculation of standard atomic volumes for RNA and comparison with proteins. RNA is packed more tightly. *J. Mol. Biol.* **346,** 477–492
29. Swift, J., Butts, C. A., Cheung-Lau, J., Yerubandi, V., and Dmochowski, I. J. (2009) Efficient self-assembly of *Archaeoglobus fulgidus* ferritin around metallic cores. *Langmuir* **25,** 5219–5225
30. Richmond, T. J. (1984) Solvent accessible surface-area and excluded volume in proteins. Analytical equations for overlapping spheres and implications for the hydrophobic effect. *J. Mol. Biol.* **178,** 63–89
31. Wesson, L., and Eisenberg, D. (1992) Atomic solvation parameters applied to molecular-dynamics of proteins in solution. *Protein Sci.* **1,** 227–235
32. Butts, C. A., Swift, J., Kang, S. G., Di Costanzo, L., Christianson, D. W., Saven, J. G., and Dmochowski, I. J. (2008) Directing noble metal ion chemistry within a designed ferritin protein. *Biochemistry* **47,** 12729–12739
33. Tosha, T., Behera, R. K., Ng, H. L., Bhattasali, O., Alber, T., and Theil, E. C. (2012) Ferritin protein nanocage ion channels. Gating by N-terminal extensions. *J. Biol. Chem.* **287,** 13016–13025
34. Theil, E. C. (2011) Ferritin protein nanocages use ion channels, catalytic sites, and nucleation channels to manage iron/oxygen chemistry. *Curr. Opin. Chem. Biol.* **15,** 304–311
35. Bertini, I., Lalli, D., Mangani, S., Pozzi, C., Rosa, C., Theil, E. C., and Turano, P. (2012) Structural insights into the ferroxidase site of ferritins from higher eukaryotes. *J. Am. Chem. Soc.* **134,** 6169–6176
36. Takagi, H., Shi, D., Ha, Y., Allewell, N. M., and Theil, E. C. (1998) Localized unfolding at the junction of three ferritin subunits. A mechanism for iron release? *J. Biol. Chem.* **273,** 18685–18688
37. Jin, W., Takagi, H., Pancorbo, B., and Theil, E. C. (2001) "Opening" the ferritin pore for iron release by mutation of conserved amino acids at interhelix and loop sites. *Biochemistry* **40,** 7525–7532